JOURNAL OF MAPS
2023, VOL. 19, NO. 1, 2227205
https://doi.org/10.1080/17445647.2023.2227205

Taylor & Francis
Taylor & Francis Group

Science

Geologic map of the Terra Cimmeria-Nepenthes Mensae transitional zone, Mars – 1:1.45Million

Ángel García-Arnay

Grupo Procesos Geoambientales y Cambio Global, IUCA, Departamento de Ciencias de la Tierra, Universidad de Zaragoza, Zaragoza, Spain

ABSTRACT

A 1:1.45Million geologic map of NW Terra Cimmeria and SE Nepenthes Mensae (-5°31′–5°38′ N, 119°20′–129°55′ E) is presented here, displaying one of the highland-lowland transitional zones of Mars with greatest contrast and diversity. The Terra Cimmeria-Nepenthes Mensae Transitional Zone comprises two complex and poorly studied geologic domains bounded by the dichotomy escarpment. The map produced in this work displays nineteen geologic units and numerous geomorphic features. Detailed mapping, morphologic and morphometric analyses and Poisson model-derived ages have permitted to constrain the stratigraphy of this transitional zone and reconstruct more accurately its geological history from the Early Noachian to recent times, suggesting a significant period of fluvial activity within the Early Amazonian. The map provides insight into the processes involved in the origin and development of this transitional zone and offers a reference geologic framework for future studies in the region.

ARTICLE HISTORY
Received 8 November 2022
Revised 3 May 2023
Accepted 31 May 2023

KEYWORDS
Planetary mapping; Poisson statistics; dichotomy boundary; paleolakes; deltas; landslides

1. Introduction

Studies carried out in the highland-lowland transitional zone of Mars permit us to shed light into the geologic processes involved in the origin and evolution of the dichotomy boundary and its nearby areas, as well as to improve our understanding of the early history of Mars (e.g. Levy et al., 2007; McGill & Dimitriou, 1990; Watters, 2003a, 2003b; Watters & McGovern, 2006). This work focuses on one of the most contrasting highland-lowland transitional zones: the ancient and densely-cratered highland plateaus of the northwestern part of Terra Cimmeria, south of the dichotomy boundary, and the relatively young and poorly-cratered lowland plains of the southeastern area of Nepenthes Mensae, north of Terra Cimmeria, mapped as Middle Noachian highland unit (mNh) and Hesperian and Noachian transition unit (HNt), respectively (Tanaka et al., 2014) (Figure 1). These geologic domains in the equatorial region of Mars are bounded by the dichotomy escarpment with a local relief of ~2 km. The Terra Cimmeria-Nepenthes Mensae Transitional Zone (CNTZ), which remains as a complex and poorly studied area (e.g. Skinner & Tanaka, 2018), is characterized by: (1) tectonically-contracted areas as inferred by the occurrence of lobate scarps, ridge crests and wrinkle ridges in the Terra Cimmeria (e.g. Watters, 2003b; Watters & Robinson, 1999) and Nepenthes Mensae regions; (2) fracture-controlled linear troughs in the vicinity of the dichotomy escarpment, probably generated by extensional tectonic deformation and/or lateral spreading along the escarpment (e.g. Irwin III et al., 2004); (3) interconnected NW-SE-trending closed depressions at the foot of the dichotomy, probably related to extensional tectonics (Watters, 2003a; Watters & McGovern, 2006); and (4) pervasive residual reliefs probably related to mass-wasting processes and 'basal sapping of volatiles' in Nepenthes Mensae (Tanaka et al., 2005). Fluvio-lacustrine activity seems to have played a fundamental role in the configuration of the CNTZ, as indicated by the presence of ancient V-shaped fluvial valleys in the Cimmeria region (e.g. García-Arnay et al., 2018b; Goudge & Fassett, 2018; Irwin & Howard, 2002), as well as moderately preserved Gilbert-type deltas and alluvial fans at their mouths (e.g. de Pablo & Pacifici, 2008; García-Arnay et al., 2018a, 2018b; García-Arnay & Gutiérrez, 2020, 2023; Irwin et al., 2005; Rivera-Hernández & Palucis, 2019). Furthermore, the occurrence of putative deltas and paleoshore platforms spatially associated with closed depressions in Nepenthes Mensae suggest the presence of paleolakes (García-Arnay & Gutiérrez, 2020). The study area has been included over time in multiple geologic maps produced by the United States Geological Survey

CONTACT Ángel García-Arnay arnay@unizar.es Grupo Procesos Geoambientales y Cambio Global, IUCA, Departamento de Ciencias de la Tierra, Universidad de Zaragoza, 50009 Zaragoza, Spain

This article has been corrected with minor changes. These changes do not impact the academic content of the article.

Supplemental data for this article can be accessed here https://doi.org/10.1080/17445647.2023.2227205.

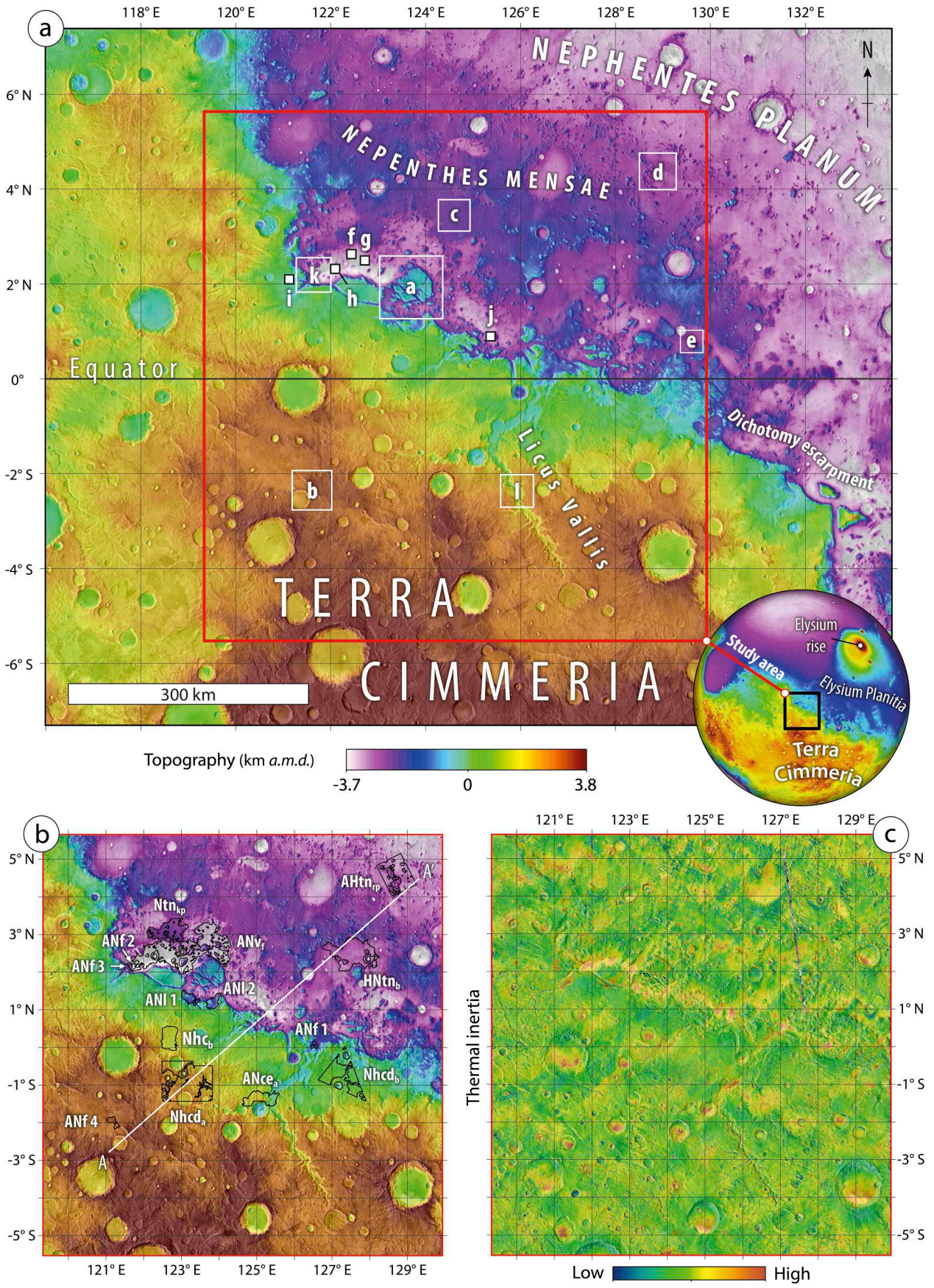

Figure 1. (a) Colorized elevation model (km above Martian datum, a.m.d.) derived from HRSC-MOLA blended data over a mosaic of THEMIS-IR day images, with the study area framed by a red rectangle. White polygons and squares indicate the location of the images of Figure 2. (b) Study area with black polygons indicating the crater-counting areas selected for dating the main surface units (Figure 4(a)). The white line indicates the trace of the geological cross-section (A-A') (Figure 5). (c) Qualitative THEMIS-derived TI mosaic of the study area over THEMIS-IR day images.

(USGS) (e.g. Greeley & Guest, 1987; Hiller, 1979; King, 1978; Scott & Carr, 1978; Tanaka et al., 1992; Tanaka et al., 2005; Tanaka et al., 2014). However, the scale of these maps precludes the representation of important features. Recently, several regional-scale geologic maps have been produced surrounding the CNTZ: the transitional zone between Terra Cimmeria and Utopia Planitia by Skinner and Tanaka (2018), northwest of the study area, providing a reference framework to compare with the CNTZ, and Aeolis Dorsa by Burr et al. (2021), southeast of the mapped area in this work. Furthermore, García-Arnay and Gutiérrez (2023) carried out a local- and regional-scale geological study in the central sector of the CNTZ, representing about 35% of the area mapped in this work. This study provided insight into the endogenic and exogenic processes involved in the configuration of this part of the CNTZ, including a geological-geomorphological map that comprises 18 geologic units.

This work presents a detailed regional-scale geological map of NW Terra Cimmeria and SE Nepenthes Mensae providing insight into the processes involved in the configuration of this transitional zone, focusing on (1) the identification, description and interpretation of the different geologic units and geomorphic features; (2) the estimation of the chronology of the main surface units; and (3) the reconstruction of the protracted geological-geomorphological history.

2. Data and methods

2.1 Imagery and topographic data

The utilized visible imagery comprised the global CTX image mosaic acquired by the Context Camera (CTX, 5–6 m/pixel) (Dickson et al., 2018; Malin et al., 2007), and additional images from the High Resolution Imaging Science Experiment (HiRISE, ~25–50 cm/pixel) (McEwen et al., 2007), both instruments on board NASA's Mars Reconnaissance Orbiter. Infrared imagery included the daytime infrared image mosaic obtained by the Thermal Emission Imaging System (THEMIS, 100 m/pixel) (Christensen et al., 2004, 2013), on board NASA's Mars Odyssey. The qualitative mosaic of the THEMIS-based thermal inertia (TI) (Fergason et al., 2006), which is derived from THEMIS nighttime infrared images, was used to differentiate surface materials (Figure 1(c)).

Topographic data were extracted from Digital Elevation Models (DEMs) derived from the Mars Orbiter Laser Altimeter (MOLA, 463 m/pixel) (Zuber et al., 1992), on board NASA's Mars Global Surveyor, as well as from the High Resolution Stereo Camera (HRSC, 50–75 m/pixel), on board ESA's Mars Express. A HRSC and MOLA blended DEM (Fergason et al., 2018, ~200 m/pixel) was used to cover areas where HRSC data are not available. In order to map the geologic units and landforms, establish their geometrical relationships, and carry out morphological and morphometric analyses, data were integrated into a Geographic Information System (Esri's ArcGIS 10.5.1) and projected into the geographic coordinate system 'GCS_Mars_2000_Sphere', with an equidistant cylindrical projection and a central meridian of 125°E.

2.2 Mapping methods

The geologic map was produced applying methodologies and techniques widely used in planetary geological mapping (e.g. Greeley & Batson, 1990; Wilhelms, 1990), and in geological mapping of Mars (e.g. Skinner & Tanaka, 2003; Skinner & Tanaka, 2018; Tanaka et al., 2014). Visible and infrared imagery together with topographic data were used to identify, interpret and correlate the surface units, largely on the basis of their primary surface features (Skinner & Tanaka, 2003). The THEMIS daytime infrared images were used as a primary base map, whereas CTX and HiRISE images, as well as the TI mosaic, were used as supplementary datasets. The name of the mapped units was based on their geographic location, where applicable, prevalent features and/or origin, as well as stratigraphic relationships (Hansen, 2000; Skinner & Tanaka, 2018; Tanaka et al., 2005). The drainage network was drawn automatically applying the 'Hydrology' toolset in ArcGIS, and later improved by removing manually artifacts using visible imagery and TI data. The proximal edges of fan-shaped features were delineated where the paleoflows debouching from the valleys used to become unconfined (García-Arnay & Gutiérrez, 2020). All crater rims >5 km in diameter have been mapped. The different preserved components of craters ≥13 km in rim diameter were depicted in the map. However, the 'Crater unit – undivided', which comprises well-preserved crater materials with rim diameters between 5 and 13 km, does not distinguish among crater-related components due to their relatively small size compared to the map scale. Azimuth data from selected mapped landforms were plotted on rose diagrams with the GeoRose 0.5.1 software (Yong Technology Inc.) (Figure 3).

2.3 Chronology of surface units

The chronological ascription of map units was addressed from the formation age estimates derived from crater size-frequency distributions and their geometrical relationships (see Figure 4). Crater populations for each unit of interest were mapped and computed using the 'CraterTools' toolset for Esri's ArcGIS (Kneissl et al., 2011). All primary craters larger than 50 or 100 m in rim diameter with centroids within the count area were mapped. Crater-counting areas larger than 1000 km^2 were selected, where

possible, to minimize the potential bias related to the variable cratering pattern (Warner et al., 2015). Surfaces occupied by well-preserved ejecta blankets were excluded from the count areas, except when it was necessary to estimate the formation age of the associated impact event. Cumulative crater size-frequency diagrams for each sampling area were generated using the CraterStats2 software (Michael & Neukum, 2010), and the absolute model ages were derived from chronology and crater production functions defined by Hartmann (2005). Age estimates were determined using a different method from the one applied in García-Arnay and Gutiérrez (2023) to obtain more confident results, mostly with model ages derived from smaller counting areas. This approach uses the Poisson timing analysis technique, which expresses the result as a probability function that incorporates inherent uncertainty, as well as the μ function (Michael et al., 2016), instead of the binning/best-fit approaches used by García-Arnay and Gutiérrez (2023).

3. Geologic units of the CNTZ

The map differentiates 19 units (18 out of them previously described by García-Arnay & Gutiérrez, 2023) that have been grouped according to their geographic distribution (see the geological map in 'Supplementary material'). Three units have been identified in the Cimmeria region of the highland province: The Cimmeria dissected units include two well-differentiated members with rugged and heavily cratered surfaces dissected by V-shaped valleys (e.g. Skinner & Tanaka, 2018; Tanaka et al., 2005, 2014). Member a ($Nhcd_a$) occurs in the topographically higher sector, whereas member b ($Nhcd_b$) crops out in the plateau situated south of the dichotomy, at lower elevation than member a, forming residual reliefs (knobs and mesas) in the transitional province (Figure 2(a)). Member a ($Nhcd_a$) shows a higher crater density than member b, NW-SE-striking lobate scarps, and less commonly ridge crests (Figure 2(b)). Member b ($Nhcd_b$) with a gradational boundary with the older member $Nhcd_a$ is characterized by localized NE-SW-oriented ridge crests, and scarce occurrence of lobate scarps with NW-SE orientation. It shows deeper valleys with a dominant NE-SW orientation, and a secondary NW-SE trend near the dichotomy boundary. The Cimmeria basin unit (Nhc_b) is a moderately cratered unit that occurs in depressions inset into member $Nhcd_a$, exhibiting smooth surfaces, wrinkle ridges, and absence of channels (Figure 2(b)).

Three units have been recognized in the Nepenthes Mensae region of the transitional province: The Nepenthes knobby plateau unit (Ntn_{kp}) is a moderately cratered unit that occurs in the inter-crater plateaus of Nepenthes Mensae, characterized by knobby terrains with residual hills made up of materials of the unit $Nhcd_b$ and mass-wasted materials (e.g. Tanaka et al., 2005) (Figure 2(c)). This unit, with a gradational boundary with the older unit $Nhcd_b$ and the younger unit $HNtn_b$, shows NW-SE-trending lobate scarps and yardangs with pervasive NW-SE orientation. The Nepenthes basin unit ($HNtn_b$) crops out in the NW-SE-trending closed depressions at the foot of the dichotomy escarpment, which used to host paleolakes (García-Arnay & Gutiérrez, 2020; Rivera-Hernández & Palucis, 2019), as well as on floors of poorly-preserved impact basins. The Nepenthes basin unit, which overlies unit $Nhcd_b$, is characterized by a lower crater density than unit Ntn_{kp}, and relatively smooth terrains locally interrupted by residual reliefs, wrinkle ridges, pitted cones and small tholi. The Nepenthes ridged plain unit ($AHtn_{rp}$) that occurs in the northeast sector of the map exhibits undulating, low-lying plains with pervasive NW-SE-oriented wrinkle ridges and scattered knobs of unit $Nhcd_b$ (Figure 2(d)). This unit, which is less-cratered than units Ntn_{kp} and $HNtn_b$, overlies unit $Nhcd_b$ and grades into the older unit Ntn_{kp}.

Seven impact crater units have been distinguished. Well-preserved craters with rim diameter between 5 and 13 km were mapped as the crater unit–undivided (AHc_u). This unit is frequently characterized by hummocky crater floors with rare occurrence of central peak or pit, and lobate ejecta deposits. The preserved morpho-structural components of moderately to well-preserved impact craters with rim diameter ≥13 km were mapped: The crater floor unit (ANc_f) is characterized by smooth, near-planar surfaces, frequently displaying a central peak and/or pit in the center of the crater (Figure 2(b)). The crater peak unit (ANc_p) shows hills with irregular and grooved surfaces, and frequent occurrence of central pits. The crater wall unit (ANc_w) comprises scarps, discontinuous terraces, blocks, and rockfalls with locally rugged surfaces. The rim crater unit (ANc_r) is formed by inward-facing scarps frequently dissected by gullies. The crater ejecta units include two morpho-facies: (1) the crater ejecta unit–facies a ($ANce_a$), which represents the inner unit characterized by rugged lobes with flowbands, and (2) the crater ejecta unit–facies b ($ANce_b$) corresponds to the distal deposits that are formed by smooth flow-oriented lobes (Figure 2(e)).

Six spatially-dispersed units have been mapped: The volcanic flow unit (ANv_f), which crops out in the deeper areas of the depressions of Nepenthes Mensae, and locally in the highlands near the dichotomy. It exhibits smooth to rugged, poorly-cratered surfaces, often with channels, overlapping lobes, and NE-SW-striking wrinkle ridges (Figure 2(f–i)). This unit locally grades into the coeval unit ANv_e, locally overlies units $HNtn_b$ and $Nhcd_b$, and underlies unit ANf. The volcanic edifice unit (ANv_e), which is laterally associated

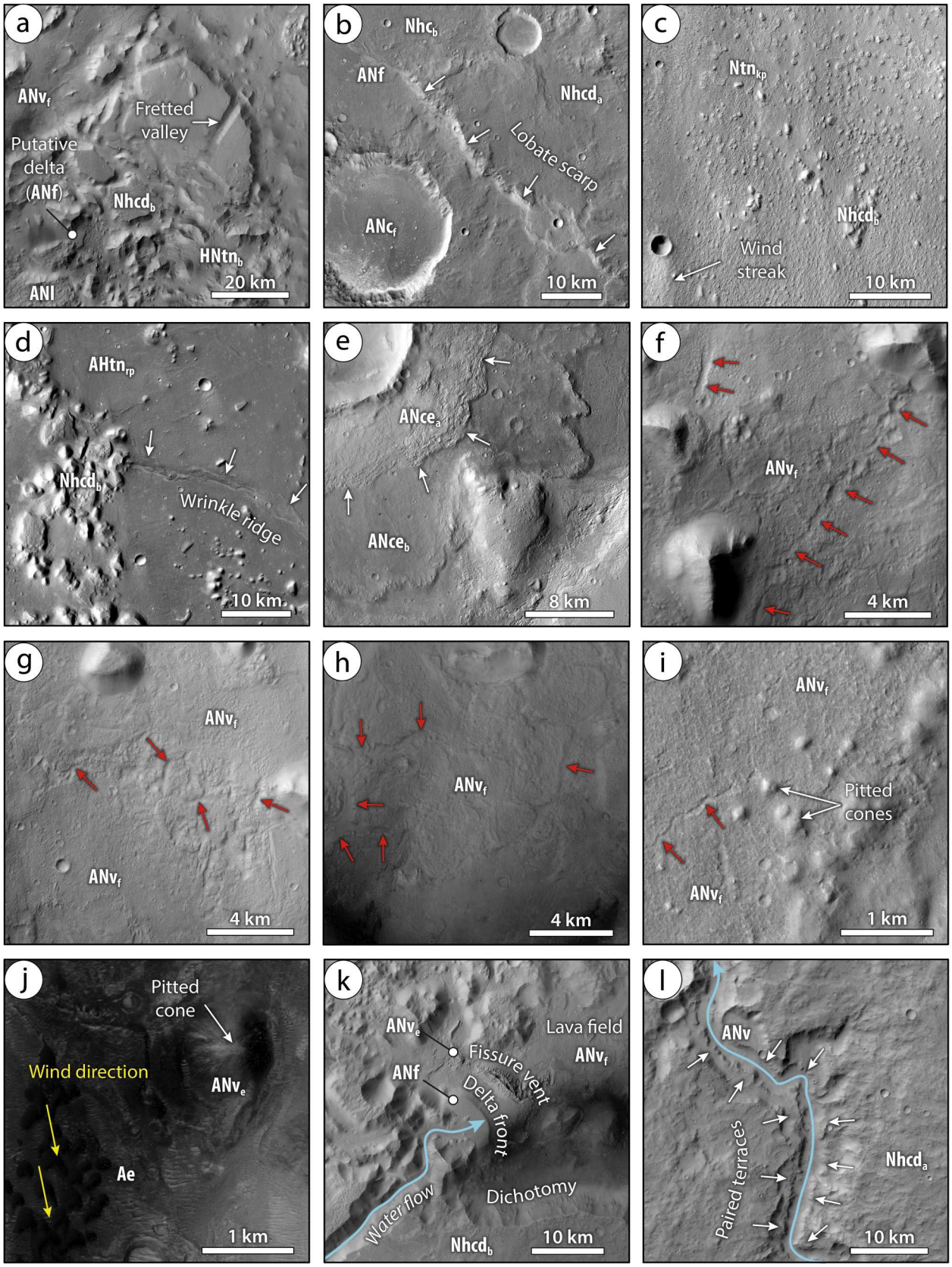

Figure 2. CTX images showing remarkable landforms in the CNTZ (locations indicated in Figure 1(a)). (a) Mesa-like landform in a megalandslide dissected by troughs related to fracture-controlled gravitational extension. (b) SW-facing lobate scarp attributable to a surface-rupturing thrust fault occurring in unit $Nhcd_a$. (c) Knobby terrain of unit Ntn_{kp} displaying wind streaks. (d) Tectonically-contracted plains of unit $AHtn_{rp}$ exhibiting wrinkle ridges and knobs. (e) Morpho-facies $ANce_a$ and $ANce_b$ related to the crater located at 129°E, 1°N. (f-h) Volcanic plains of unit ANv_f exhibiting probable collapse lava tubes. (i) Volcano-like pitted cones of unit ANv_e and probable collapse lava tubes of unit ANv_f. (j) Volcano-like pitted cone of unit ANv_e and dark-tone barchan dune fields of unit Ae. (k) Putative Gilbert-type delta and volcanic features such as fissure vents and lava fields. (l) Paired terraces in Licus Vallis. North is up in all images.

with unit ANv_f, is characterized by isolated and coalesced raised fissures with sloping, and rugged to smooth surfaces, as well as small cone- and mound-shaped features (Figure 2(i–k)). The valley unit (ANv) that is carved in units $Nhcd_a$ and $Nhcd_b$, and rarely in unit Ntn_{kp} displays smooth deposits underlying the low-TI valley floors (Figure 2(k, l)). The fan unit (ANf), which is laterally associated with unit ANv, is related to fan-shaped deposits with smooth to corrugated surfaces due to differential erosion (Figure 2(k)). The landslide unit (ANl) mostly occurs associated with the dichotomy escarpment locally overlying units $Nhcd_b$ and $HNtn_b$. It is characterized by rugged, rolling, and hummocky terrains. The eolian unit (Ae) consists of dark-tone, barchan and longitudinal dune fields occurring near the foot of the dichotomy, and locally overlying units ANv_f, ANc_f, ANv, $HNtn_b$ and $Nhcd_b$ (Figure 2(j)).

4. Geomorphic features

The main landforms that occur within the geological units have also been mapped. Two types of scarps were differentiated: (1) Lobate scarps are linear to sinuous, NW-SE-oriented ridge-like landforms (Figure 3(a)) showing asymmetric transverse profiles with convex and SW-facing scarps (e.g. Watters & Robinson, 1999) (Figure 2(b)). These landforms mostly occur

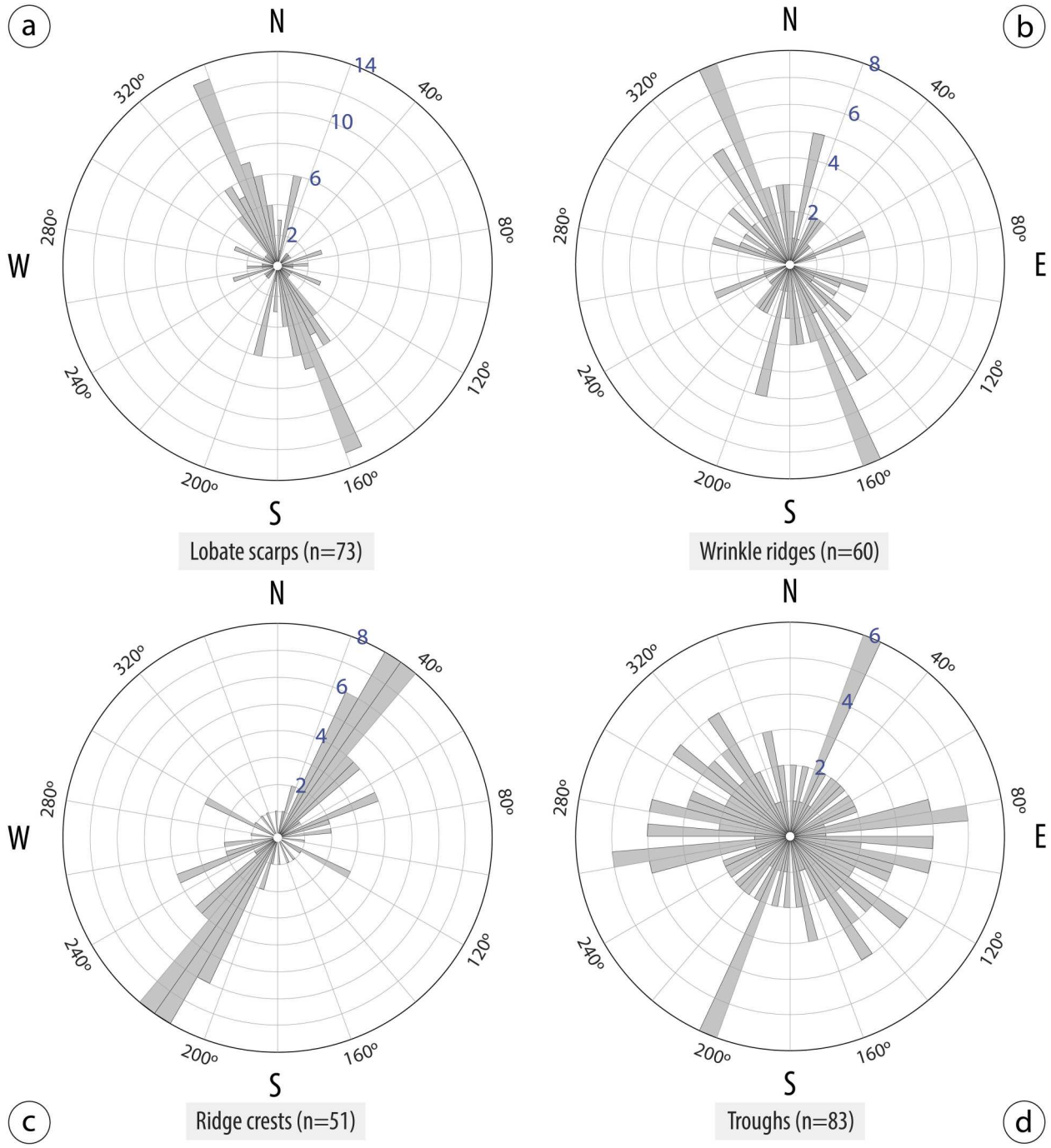

Figure 3. Rose diagrams displaying the distribution of the orientation of lobate scarps (a), wrinkle ridges (b), ridge crests (c), and troughs (d). n: number of features.

in units $Nhcd_a$, $Nhcd_b$ and Ntn_{kp}. Lobate scarps often disrupt valleys and pre-existing crater floors. (2) The linear to sinuous dichotomy escarpment ca. 2 km high, which is dissected by numerous valleys in unit $Nhcd_b$ (Figure 2(k)). The escarpment shows a dominant NW-SE orientation that turns into a N-S trend in the western sector of the map.

Four types of ridges have been recognized: (1) Wrinkle ridges are linear to curvilinear ridges with crenulated crests, and asymmetric cross profiles (e.g. Watters, 1988) (Figure 2(d)). These landforms show a NW-SE orientation within units Nhc_b and $HNtn_b$, and a NE-SW trend in the unit ANv_f (Figure 3(b)). (2) Ridge crests are ridges that display a near-symmetric transverse profile (e.g. Watters et al., 2009). They frequently occur in units $Nhcd_a$ and $Nhcd_b$ with a dominant NE-SW orientation, and a secondary NW-SE trend (Figure 3(c)). (3) Volcanic ridges are linear to curvilinear ridges related to fissure vents in unit ANv_e that display smooth to rugged slopes, and weak NE-SW and NW-SE prevalent orientations. (4) Channel ridges, often known as 'inverted channels', related to relief inversion by differential erosion are characterized by a sinuous pattern and scarcely occur in valley floors and fans (e.g. Burr et al., 2010).

Four types of negative relief morphologies were distinguished: (1) Troughs are linear to curvilinear steep-walled depressions (Figure 2(a)). These landforms, which form a distinctive polygonal pattern with a dominant NW-SE orientation and a secondary NE-SW trend (Figure 3(d)), occur in the vicinity of the dichotomy cutting into unit $Nhcd_b$. (2) Valleys are networks of V-shaped, steep-walled depressions with linear to sinuous trace and dendritic to trellis pattern (Figure 2(k, l)). Their path seems to be locally controlled by lobate scarps, ridge crests and troughs, with evidence of deflections. (3) Channels are linear to sinuous, shallow and narrow depressions occurring in the valley floors, locally with positive relief sections. The channel networks mostly occur in units $Nhcd_a$ and $Nhcd_b$ and scarcely in unit Ntn_{kp}. They exhibit an orthogonal pattern with a dominant NE-SW orientation, and a secondary NW-SE trend, probably controlled by fractures. It is common the occurrence of knickpoints, as well as defeated and beheaded channels. (4) Pit craters are elongated, closed depressions with scarped boundaries (e.g. Parenti et al., 2020). The major axis of these features that locally occur in unit ANv_f display a predominant NW-SE orientation.

Two types of mound- and cone-shaped landforms associated with unit ANv_e were mapped: (1) Pitted cones are conical hills with smooth slopes and central pits (e.g. Skinner & Tanaka, 2018) (Figure 2(i, j)). These landforms occur in unit ANv_f, and less frequently in units Ntn_{kp} and $HNtn_b$. (2) Small tholi, which generally occur in unit ANv_f and rarely in unit $HNtn_b$, are mounds often exhibiting central peaks and subtle outward-facing slopes bounded by marginal scarps (e.g. Skinner & Tanaka, 2018).

5. Age estimates

In order to obtain estimates of the surface age of the main map units, the crater size-frequency distribution was analyzed in 14 counting areas (see Figure 4(a) and Appendix – Figure A1). In the highland province, average formation age estimates of μ3.99 ± 0.05/0.06 Ga (Early to Middle Noachian) and μ3.89 ± 0.04/0.04 Ga (Middle Noachian) were obtained for units $Nhcd_a$ and $Nhcd_b$, respectively, and μ3.59 ± 0.02/0.03 Ga (Late Noachian) for unit Nhc_b, considering crater-counting areas of ~4,600, ~1,800 and ~790 km^2, respectively. In the transitional province, units Ntn_{kp}, $HNtn_b$ and $AHtn_{rp}$ yielded average formation ages of μ3.71 ± 0.04/0.05 Ga (Late Noachian), μ3.55 ± 0.07/0.10 Ga (Late Noachian to Early Hesperian), and μ3.25 ± 0.14/0.33 (Late Hesperian to Early Amazonian), using counting areas of ~1,200, ~2,400 and ~1,800 km^2, respectively. Among the spatially-dispersed units, the unit ANv_f yielded an average formation age of μ1.74 ± 0.18/0.18 Ga (Early Amazonian) considering a counting area of ~9,000 km^2. Four counting areas were selected for unit ANf, located in the largest putative deltas and alluvial fans in the CNTZ (deltas referred to as 'D2' (see Figure 2(k)) and 'D7' by García-Arnay and Gutiérrez (2020)). Putative deltas 'D7' and 'D2' (lower and upper surfaces) yielded, respectively, average formation age estimates of μ3.51 ± 0.10/0.20 Ga (Late Noachian to Late Hesperian), μ3.12 ± 0.45/0.93 Ga (Late Noachian to Early Amazonian; lower delta 'D2') and μ2.07 ± 0.37/0.37 Ga (Early Amazonian; upper delta 'D2'), with corresponding counting areas of ~85.4, ~53, and ~41.1 km^2 (areas ANf 1, ANf 2 and ANf 3, respectively). The largest alluvial fan yielded an average formation age estimate of μ3.14 ± 0.18/0.34 Ga (Late Hesperian to Early Amazonian), with a counting area of ~166.2 km^2 (area ANf 4). Two counting areas of ~318 and ~314 km^2 (areas ANl 1 and ANl 2, respectively) were considered for unit ANl, with average formation age estimates of μ0.78 ± 0.29/0.23 Ga (Early to Middle Amazonian) and μ0.66 ± 0.16/0.14 Ga (Middle Amazonian), respectively. A minimum age estimate for the cessation of fluvial activity in the main valley of Licus Vallis was obtained analyzing the crater size-frequency distribution of the crater population developed on the ejecta deposits of unit $ANce_a$ that overlap the middle course of the valley. These deposits do not exhibit any evidence of reworking by fluvial activity. Considering a counting area of ~860 km^2, it was estimated a minimum age for the cessation of fluvial activity of μ3.31 ± 0.09/0.18 Ga (Early Hesperian to Early Amazonian).

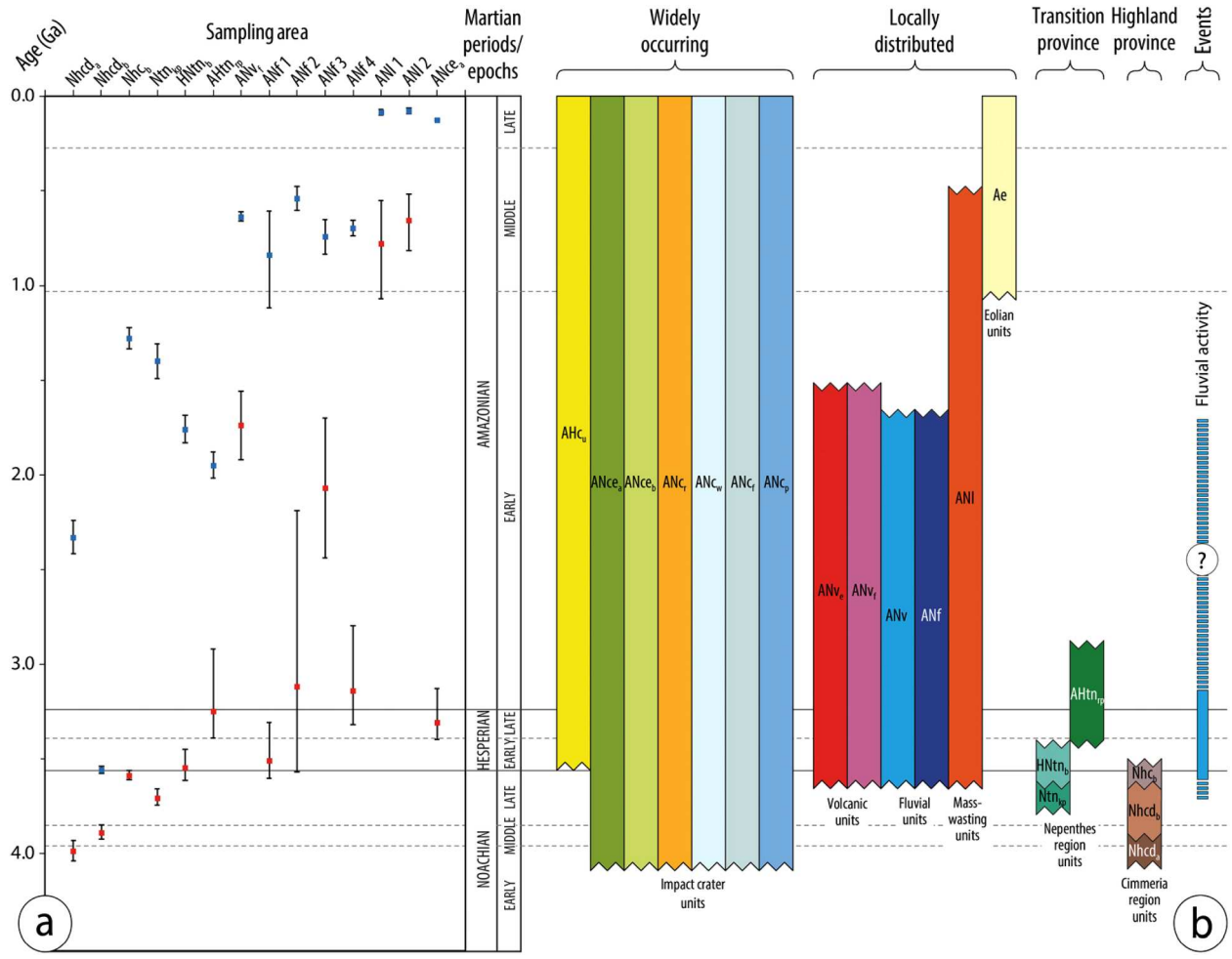

Figure 4. (a) Diagram showing age estimates (red and blue boxes for formation and resurfacing ages, respectively), and their error bars (vertical black lines) from the crater size-frequency diagrams for the main mapped units (see Figure A1). (b) Correlation of map units based on ages estimated by crater counting and geometrical relationships between units. Hachured polygon borders indicate possible, extended durations. Horizontal continuous and dashed lines indicate the boundaries between the Martian geological periods and epochs, respectively (Michael, 2013).

The obtained age estimates using the Poisson timing analysis method are generally younger and have larger error ranges compared to those estimated in García-Arnay and Gutiérrez (2023) for smaller counting areas (e.g. the fan unit). In contrast, age estimates obtained for larger counting areas generally show consistency with both approaches.

6. Interpretation and correlation of map units

The interpretation of the geologic units and landforms and their chronological ascription, based on both geometrical relationships and crater counts, is summarized here (see Figures 4 and 5).

6.1 Early to Middle Noachian epochs

The documented stratigraphic record of the CNTZ began in the Early to Middle Noachian, with the emplacement of units $Nhcd_a$ and $Nhcd_b$ in the Cimmeria region, interpreted as moderately to heavily degraded undifferentiated highland materials related to impact, volcanic, basin-fill, and fluvial processes. Both units form part of the unit mNh (Middle Noachian) defined by Tanaka et al. (2014). The unit $Nhcd_b$ possibly also correlates with unit Nhc_1 (Early to Middle Noachian) mapped by Skinner and Tanaka (2018). The widespread occurrence of lobate scarps related to thrust faults (e.g. Watters & Robinson, 1999) suggests that these units were affected by NE-SW-oriented tectonic shortening (García-Arnay & Gutiérrez, 2023).

6.2 Late Noachian epoch

In the Late Noachian, uncertain-origin depressions inset into unit $Nhcd_a$ were filled by sediments to form unit Nhc_b, consisting of slightly to moderately degraded undifferentiated deposits probably related to fluvial, basin-fill and impact processes. This tectonically contracted unit, as inferred by wrinkle ridges attributed to thrust faults (e.g. Andrews-Hanna, 2020), likely correlates with unit lNh (Late Noachian)

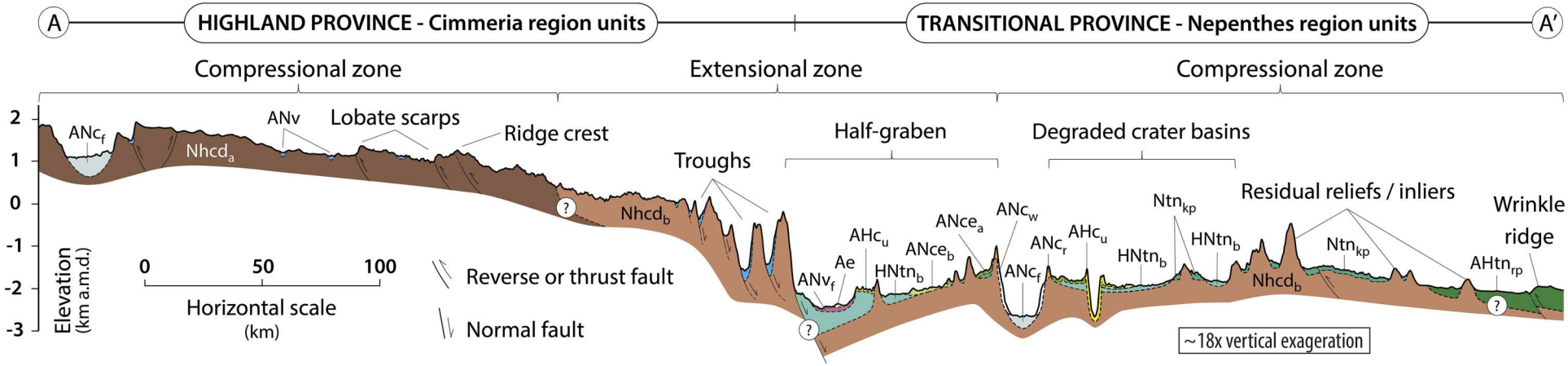

Figure 5. Geological cross-section A-A′ (see location in Figure 1(b)) constructed on the basis of cartographic relationships and crater-counting-based ages (Figure 4).

defined by Tanaka et al. (2014). The Nepenthes Mensae region is characterized by knobby terrains, probably generated by basal sapping and mass-wasting processes (Tanaka et al., 2005), as well as a belt of large extensional depressions and troughs (e.g. Watters, 2003a). The unit Ntn_{kp} is probably formed by undifferentiated materials attributed to volcanic and impact products, and mass-wasted deposits forming aprons around knobs and mesas of the unit $Nhcd_b$. This tectonically contracted unit, with morphotectonic features indicating a NE-SW shortening trend, was formed during the Late Noachian. According to García-Arnay and Gutiérrez (2023), the extensional tectonics, which seems to begin during the Late Noachian, probably led to the development of: (1) the 2-km-high dichotomy boundary interpreted as a fault scarp related to a master normal fault. (2) The system of interconnected NW-SE-trending closed depressions in Nepenthes Mensae. These basins appear to correspond to keystone grabens associated with the master fault of a larger half-graben morpho-structure featuring a rollover anticline. (3) The plateau located to the south of the dichotomy boundary in Terra Cimmeria with down-to-the-north topographic drops associated with secondary normal faults. (4) The fissure-type volcanism in the deepest areas of the depressions in Nepenthes Mensae. (5) The mega landslides derived from the dichotomy escarpment.

6.3. Hesperian period

The locally contracted unit $HNtn_b$, that is probably underlain by lacustrine, fluvial, and mass-wasted materials ascribed to the Late Noachian and Early Hesperian, is related to the paleolake basins (e.g. García-Arnay & Gutiérrez, 2020). The units Ntn_{kp} and $HNtn_b$ are integrated into unit HNt (Noachian and Hesperian periods) by Tanaka et al. (2014). The units Nhc_2 (Middle to Late Noachian) and $HNhc_3$ (Late Noachian to Early Hesperian) defined by Skinner and Tanaka (2018) may correlate with the mapped units Ntn_{kp} and $HNtn_b$, respectively.

6.4. Early Amazonian epoch

From the Late Noachian, fluvial activity started to carve units $Nhcd_a$ and $Nhcd_b$ to form the valley networks and associated putative deltas and alluvial fans corresponding to units ANv and ANf, respectively, most probably lasting up to Early Amazonian times, as suggested by the formation ages obtained for the most of the analyzed fans/deltas. These age estimates are younger in comparison with those published by García-Arnay and Gutiérrez (2023). Fluvial valleys are locally disrupted by thrust faults and transformed into beheaded drainages. The unit $AHtn_{rp}$, formed during Late Hesperian to Early Amazonian times, consists of tectonically contracted materials related to impact, mass-wasting, fluvio-lacustrine and volcanic processes. It likely correlates with the unit eHt (Early Hesperian) defined by Tanaka et al. (2014). The units ANv_e and ANv_f are ascribable to different types of volcanic edifices and high-TI lava fields, respectively. Pitted cones exhibit a geometric shape similar to mud volcanoes reported in the northern plains. However, their spatial association with the volcanic flow unit (ANv_f) and fissure vents suggests a hydrovolcanic origin (e.g. tuff cones), as also indicated by Brož and Hauber (2013) in and around Nepenthes Planum region. These genetically-linked units, which are integrated into unit HNt of Tanaka et al. (2014), were coevally emplaced from Late Noachian to Early Amazonian times, suggesting that the extensional phase may have even been active until Early Amazonian times.

6.5. Middle to Late Amazonian epochs

The unit ANl consists of deposits related to large landslides (e.g. rock spreads, slumps and falls) that were probably accumulated from the Late Noachian to the Middle Amazonian. Through the Amazonian period, eolian activity formed the dune fields of unit Ae, as well as erosional landforms like yardangs and wind streaks, indicating a persistent SE-directed wind.

7. Conclusions

The production of the 1:1.45M geologic map of the NW Terra Cimmeria and SE Nepenthes Mensae has permitted to (1) constrain the stratigraphy of this poorly explored highland-lowland transitional zone of Mars, differentiating nineteen geologic units that include a wide variety of geomorphic features; and (2) reconstruct its long-term geological history that ranges from the Early Noachian to recent times. The Poisson model-derived ages generally show consistency with those estimated by binning/best-fit approaches for larger counting areas. In contrast, significant younger age estimates were obtained for smaller counting areas. The mapping has also shed light on the role played by the inferred compressional and extensional tectonics, as well as the fluvio-lacustrine activity on the configuration of the landscape in the CNTZ from Late Noachian to Early Amazonian. This work provides a detailed geologic framework for future studies within this transitional zone, of special interest from the paleohydrological perspective and for understanding the evolution of early Mars.

Software

Esri's ArcGIS 10.5.1 was used for mapping, performing multiple analyses and generate the layout of the

map. The final editing of the map was carried out using Adobe Illustrator CS6 and Adobe Photoshop CS4. Azimuth data were plotted with the GeoRose 0.5.1 software (Yong Technology Inc.). 'CraterTools' toolset for Esri's ArcGIS (Kneissl et al., 2011) and 'CraterStats2' software (Michael & Neukum, 2010) were used to map and compute the crater populations, and generate the crater size-frequency diagrams, respectively.

Acknowledgments

I am very grateful to Prof. Francisco Gutiérrez (Universidad de Zaragoza, Spain) for his supervision and endless scientific support to carry out this work, as well as for the review of the manuscript. I would also like to express my gratitude to Dr. Gian Gabriele Ori and Dr. Andrea Pacifici for their hospitality and support during my research stay at the IRSPS, as well as the reviewers Dr. Makram Murad-al-shaikh, Dr. Robert C. Anderson and Dr. Solmaz Adeli, and the editors, Dr. Monica Pondrelli and Dr. Mike J. Smith, for their valuable suggestions and comments, which helped to improve this paper. This work has been sponsored by the Instituto Universitario de Investigación en Ciencias Ambientales de Aragón (IUCA).

Disclosure statement

No potential conflict of interest was reported by the author(s).

Funding

This research was supported by a PhD scholarship granted to ÁG-A (ref. C237/2016) by the Gobierno de Aragón (Spain) and the European Social Fund, as well as by grants awarded by the Ibercaja-CAI mobility programme (ref. CB 2/21; Universidad de Zaragoza, Fundación Bancaria Ibercaja and Fundación CAI) and the Erasmus + Traineeship programme (ref. 53971; European Commission) to fund a research stay of ÁG-A at the International Research School of Planetary Sciences (Università degli Studi 'G. D'Annunzio', Italy).

Data availability statement

The input data that support this work are freely available from these resources: (1) The PDS Geosciences Node Mars Orbital Data Explorer at [https://ode.rsl.wustl.edu/mars/index.aspx]; (2) The THEMIS-IR Day Global Mosaic of Mars at [https://astrogeology.usgs.gov/search/map/Mars/Odyssey/THEMIS-IR-Mosaic-ASU/Mars_MO_THEMIS-IR-Day_mosaic_global_100m_v12]; (3) The Mars THEMIS-Derived Global Thermal Inertia Mosaic at [https://astrogeology.usgs.gov/maps/mars-themis-derived-global-thermal-inertia-mosaic]; (4) The CTX Global Mosaic of Mars at [http://murray-lab.caltech.edu/CTX/]; and (5) The Mars HRSC and MOLA Blended Digital Elevation Model at [http://bit.ly/HRSC_MOLA_Blend_v0].

ORCID

Ángel García-Arnay http://orcid.org/0000-0002-4899-680X

References

Andrews-Hanna, J. C. (2020). The tectonic architecture of wrinkle ridges on Mars. *Icarus*, *351*, 113937. https://doi.org/10.1016/j.icarus.2020.113937

Brož, P., & Hauber, E. (2013). Hydrovolcanic tuff rings and cones as indicators for phreatomagmatic explosive eruptions on Mars. *Journal of Geophysical Research: Planets*, *118*(8), 1656–1675. https://doi.org/10.1002/jgre.20120

Burr, D., Jacobsen, R. E., Lefort, A., Borden, R. M., & Peel, S. E. (2021). Geologic Map of the Aeolis Dorsa Region, Mars. *US Department of the Interior, US Geological Survey*, https://doi.org/10.3133/sim3480

Burr, D. M., Williams, R. M., Wendell, K. D., Chojnacki, M., & Emery, J. P. (2010). Inverted fluvial features in the Aeolis/Zephyria Plana region, Mars: Formation mechanism and initial paleodischarge estimates. *Journal of Geophysical Research: Planets*, *115*(E7), https://doi.org/10.1029/2009JE003496

Christensen, P. R., Fergason, R. L., Edwards, C. S., & Hill, J. (2013). THEMIS-derived thermal inertia mosaic of Mars: Product description and science results. *Lunar and Planetary Science Conference Abstracts*, *44*, 2822. https://www.lpi.usra.edu/meetings/lpsc2013/pdf/2822.pdf

Christensen, P. R., Jakosky, B. M., Kieffer, H. H., Malin, M. C., McSween, H. Y., Nealson, K., Mehall, G. L., Silverman, S. H., Ferry, S., Caplinger, M., & Ravine, M. (2004). The thermal emission imaging system (THEMIS) for the Mars 2001 Odyssey Mission. *Space Science Reviews*, *110* (1–2), 85–130. https://doi.org/10.1023/B:SPAC.0000021008.16305.94

de Pablo, MÁ, & Pacifici, A. (2008). Geomorphological evidence of water level changes in Nepenthes Mensae, Mars. *Icarus*, *196*(2), 667–671. https://doi.org/10.1016/j.icarus.2008.04.005

Dickson, J. L., Kerber, L. A., Fassett, C. I., & Ehlmann, B. L. (2018). A global, blended CTX mosaic of Mars with vectorized seam mapping: A new mosaicking pipeline using principles of non-destructive image editing. *Lunar and Planetary Science Conference Abstracts*, *49*, 2480. https://murray-lab.caltech.edu/CTX/LPSC2018_CTX-Mosaic-Poster.pdf

Fergason, R. L., Christensen, P. R., & Kieffer, H. H. (2006). High-resolution thermal inertia derived from the Thermal Emission Imaging System (THEMIS): Thermal model and applications. *Journal of Geophysical Research: Planets*, *111*(E12), https://doi.org/10.1029/2006JE002735

Fergason, R. L., Hare, T. M., & Laura, J. (2018). Hrsc and MOLA blended digital elevation model at 200 m v2, astrogeology PDS annex. U.S. Geological Survey http://bit.ly/HRSC_MOLA_Blend_v0.

García-Arnay, Á, Fernández, S., de Pablo, MÁ, & Gutiérrez, F. (2018b). The dominant morphogenetic role of surface runoff in Licus Vallis, Mars: Results from geomorphological and morphometric analyses. *Geogaceta*, *63*, 63–66. http://www.sociedadgeologica.es/archivos/geogacetas/geo63/geo63_16.pdf.

García-Arnay, Á, & Gutiérrez, F. (2020). Reconstructing paleolakes in Nepenthes Mensae, Mars, using the distribution of putative deltas, coastal-like features, and terrestrial analogs. *Geomorphology*, *359*, 107129. https://doi.org/10.1016/j.geomorph.2020.107129

García-Arnay, Á, & Gutiérrez, F. (2023). Unravelling the geological and geomorphological evolution of the Terra Cimmeria-Nepenthes Mensae transitional zone, Mars. *Geomorphology*, *428*, 108641. https://doi.org/10.1016/j.geomorph.2023.108641

García-Arnay, Á, Gutiérrez, F., de Pablo, MÁ, & Fernández, S. (2018a). Characterization and interpretation of the fan-shaped and terrace-like features identified in Nepenthes Mensae, Mars. *EGU General Assembly Conference Abstracts*, *20*, 808. https://figshare.com/articles/Characterization_and_interpretation_of_the_fanshaped_and_terrace-like_features_identified_in_Nepenthes_Mensae_Mars/9824609.

Goudge, T. A., & Fassett, C. I. (2018). Incision of Licus Vallis, Mars, from multiple lake overflow floods. *Journal of Geophysical Research: Planets*, *123*(2), 405–420. https://doi.org/10.1002/2017JE005438

Greeley, R., & Batson, R. M. (1990). *Planetary mapping* (pp. 296). Cambridge Univ. Press.

Greeley, R., & Guest, J. (1987). Geologic map of the eastern equatorial region of Mars. U.S. Geological Survey, IMAP 1802, Scale 1:5,000,000. https://doi.org/10.3133/i1802B.

Hansen, V. L. (2000). Geologic mapping of tectonic planets. *Earth and Planetary Science Letters*, *176*(3–4), 527–542. https://doi.org/10.1016/S0012-821X(00)00017-0

Hartmann, W. K. (2005). Martian cratering 8: Isochron refinement and the chronology of Mars. *Icarus*, *174*(2), 294–320. https://doi.org/10.1016/j.icarus.2004.11.023

Hiller, K. H. (1979). Geologic map of the Amenthes Quadrangle of Mars. U.S. Geological Survey, IMAP 1110, Scale 1:5,000,000. https://doi.org/10.3133/i1110.

Irwin, R. P., & Howard, A. D. (2002). Drainage basin evolution in noachian terra cimmeria, Mars. *Journal of Geophysical Research: Planets*, *107*(E7), https://doi.org/10.1029/2001JE001818

Irwin, R. P., Howard, A. D., Craddock, R. A., & Moore, J. M. (2005). An intense terminal epoch of widespread fluvial activity on early Mars: 2. Increased runoff and paleolake development. *Journal of Geophysical Research: Planets*, *110*(E12), https://doi.org/10.1029/2005JE002460

Irwin III, R. P., Watters, T. R., Howard, A. D., & Zimbelman, J. R. (2004). Sedimentary resurfacing and fretted terrain development along the crustal dichotomy boundary, Aeolis Mensae, Mars. *Journal of Geophysical Research: Planets*, *109*(E9), https://doi.org/10.1029/2004JE002248

King, E. A. (1978). Geologic map of the Mare Tyrrhenum Quadrangle of Mars. US Geological Survey Report, IMAP 1073. https://doi.org/10.3133/i1073.

Kneissl, T., van Gasselt, S., & Neukum, G. (2011). Map-projection-independent crater size-frequency determination in GIS environments—new software tool for ArcGIS. *Planetary and Space Science*, *59*(11), 1243–1254. https://doi.org/10.1016/j.pss.2010.03.015

Levy, J. S., Head, J. W., & Marchant, D. R. (2007). Lineated valley fill and lobate debris apron stratigraphy in Nilosyrtis Mensae, Mars: Evidence for phases of glacial modification of the dichotomy boundary. *Journal of Geophysical Research: Planets*, *112*(E8), https://doi.org/10.1029/2006JE002852

Malin, M. C., Bell, J. F., Cantor, B. A., Caplinger, M. A., Calvin, W. M., Clancy, R. T., & Lee, S. W. (2007). Context camera investigation on board the Mars Reconnaissance Orbiter. *Journal of Geophysical Research: Planets*, *112*(E5), https://doi.org/10.1029/2006JE002808

McEwen, A. S., Eliason, E. M., Bergstrom, J. W., Bridges, N. T., Hansen, C. J., Delamere, W. A., Grant, J. A., Gulick, V. C., Herkenhoff, K. E., Keszthelyi, L., Kirk, R. L., Mellon, M. T., Squyres, S. W., Thomas, N., & Weitz, C. M. (2007). Mars reconnaissance orbiter's high resolution imaging science experiment (HiRISE). *Journal of Geophysical Research: Planets*, *112*(E5), https://doi.org/10.1029/2005JE002605

McGill, G. E., & Dimitriou, A. M. (1990). Origin of the Martian global dichotomy by crustal thinning in the late Noachian or early Hesperian. *Journal of Geophysical Research*, *95*(B8), 12595–12605. https://doi.org/10.1029/JB095iB08p12595

Michael, G. G. (2013). Planetary surface dating from crater size–frequency distribution measurements: Multiple resurfacing episodes and differential isochron fitting. *Icarus*, *226*(1), 885–890. https://doi.org/10.1016/j.icarus.2013.07.004

Michael, G. G., Kneissl, T., & Neesemann, A. (2016). Planetary surface dating from crater size-frequency distribution measurements: Poisson timing analysis. *Icarus*, *277*, 279–285. https://doi.org/10.1016/j.icarus.2016.05.019

Michael, G. G., & Neukum, G. (2010). Planetary surface dating from crater size–frequency distribution measurements: Partial resurfacing events and statistical age uncertainty. *Earth and Planetary Science Letters*, *294*(3), 223–229. https://doi.org/10.1016/j.epsl.2009.12.041

Parenti, C., Gutiérrez, F., Baioni, D., García-Arnay, Á, Sevil, J., & Luzzi, E. (2020). Closed depressions in Kotido crater, Arabia Terra, Mars. Possible evidence of evaporite dissolution-induced subsidence. *Icarus*, *341*, 113680. https://doi.org/10.1016/j.icarus.2020.113680

Rivera-Hernández, F., & Palucis, M. C. (2019). Do deltas along the crustal dichotomy boundary of Mars in the Gale crater region record a northern ocean?. *Geophysical Research Letters*, *46*(15), 8689–8699. https://doi.org/10.1029/2019GL083046

Scott, D. H., & Carr, M. H. (1978). Geologic Map of Mars: U.S. Geological Survey Investigations Series, I-1083, Scale 1:25,000,000. http://pubs.er.usgs.gov/publication/i1083.

Skinner Jr, J. A., & Tanaka, K. L. (2003). How should planetary map units be defined? *Lunar and Planetary Science Conference Abstracts*, *34*, 2100. https://www.lpi.usra.edu/meetings/lpsc2003/pdf/2100.pdf.

Skinner Jr, J. A., & Tanaka, K. L. (2018). Geological Map of the Nepenthes Planum Region, Mars. US Geological Survey Scientific Investigations Map 3389, Scale 1:1,506,000. https://doi.org/10.3133/sim3389.

Tanaka, K. L., Chapman, M. G., & Scott, D. H. (1992). Geologic map of the Elysium region of Mars. US Geological Survey Report, IMAP 2147. https://doi.org/10.3133/i2147.

Tanaka, K. L., Skinner, J. A., Dohm, J. M., Irwin, I. I. I., Kolb, R. P., Fortezzo, E. J., Platz, C. M., Michael, T., Hare, G. G., & M, T. (2014). Geologic Map of Mars. US Geological Survey Scientific Investigations Map 3292, Scale 1:20,000,000. pamphlet 43 p. https://doi.org/10.3133/sim3292.

Tanaka, K. L., Skinner, J. A., & Hare, T. M. (2005). Geologic map of the northern plains of Mars. US Geological Survey Scientific Investigations Map 2888, Scale 1:15,000,000. https://doi.org/10.3133/sim2888.

Warner, N. H., Gupta, S., Calef, F., Grindrod, P., Boll, N., & Goddard, K. (2015). Minimum effective area for high resolution crater counting of Martian terrains. *Icarus*, *245*, 198–240. https://doi.org/10.1016/j.icarus.2014.09.024

Watters, T. R. (1988). Wrinkle ridge assemblages on the terrestrial planets. *Journal of Geophysical Research*, *93*(B9), 10236–10254. https://doi.org/10.1029/JB093iB09p10236

Watters, T. R. (2003a). Lithospheric flexure and the origin of the dichotomy boundary on Mars. *Geology*, *31*(3), 271–274. https://doi.org/10.1130/0091-7613(2003)031<0271:LFATOO>2.0.CO;2

Watters, T. R. (2003b). Thrust faults along the dichotomy boundary in the eastern hemisphere of Mars. *Journal of Geophysical Research: Planets*, *108*(E6), 5054. https://doi.org/10.1029/2002JE001934

Watters, T. R., & McGovern, P. J. (2006). Lithospheric flexure and the evolution of the dichotomy boundary on Mars. *Geophysical Research Letters*, *33*(8), https://doi.org/10.1029/2005GL024325

Watters, T. R., & Robinson, M. S. (1999). Lobate scarps and the Martian crustal dichotomy. *Journal of Geophysical Research: Planets*, *104*(E8), 18981–18990. https://doi.org/10.1029/1998JE001007

Watters, T. R., Solomon, S. C., Robinson, M. S., Head, J. W., André, S. L., Hauck, I. I., Murchie, S. A., & L, S. (2009). The tectonics of Mercury: The view after MESSENGER's first flyby. *Earth and Planetary Science Letters*, *285*(3-4), 283–296. https://doi.org/10.1016/j.epsl.2009.01.025

Wilhelms, D. E. (1990). Geologic mapping. In R. Greeley, & R. M. Batson (Eds.), *Planetary mapping* (pp. 208–260). Cambridge University Press, NY.

Zuber, M. T., Smith, D. E., Solomon, S. C., Muhleman, D. O., Head, J. W., & Garvin, J. B. (1992). The Mars Observer laser altimeter investigation. *Journal of Geophysical Research: Planets*, *97*(E5), 7781–7797. https://doi.org/10.1029/92JE00341

Appendix

Figure A1. (a-n) Crater size-frequency diagrams for each counting area (see locations in Figure 1(b)). Absolute model ages measured by Poisson calculation indicating the formation ages (red fit lines), and the resurfacing events (blue fit lines). The 'μ' function represents the uncertainty of calibration of the particular chronology model (Michael et al., 2016). The grey shadow bands represent the time boundaries between the different Martian geological epochs (Michael, 2013). 'D_{min}' and 'n' refer to the minimum crater diameter and the number of counted craters for each counting area, respectively.